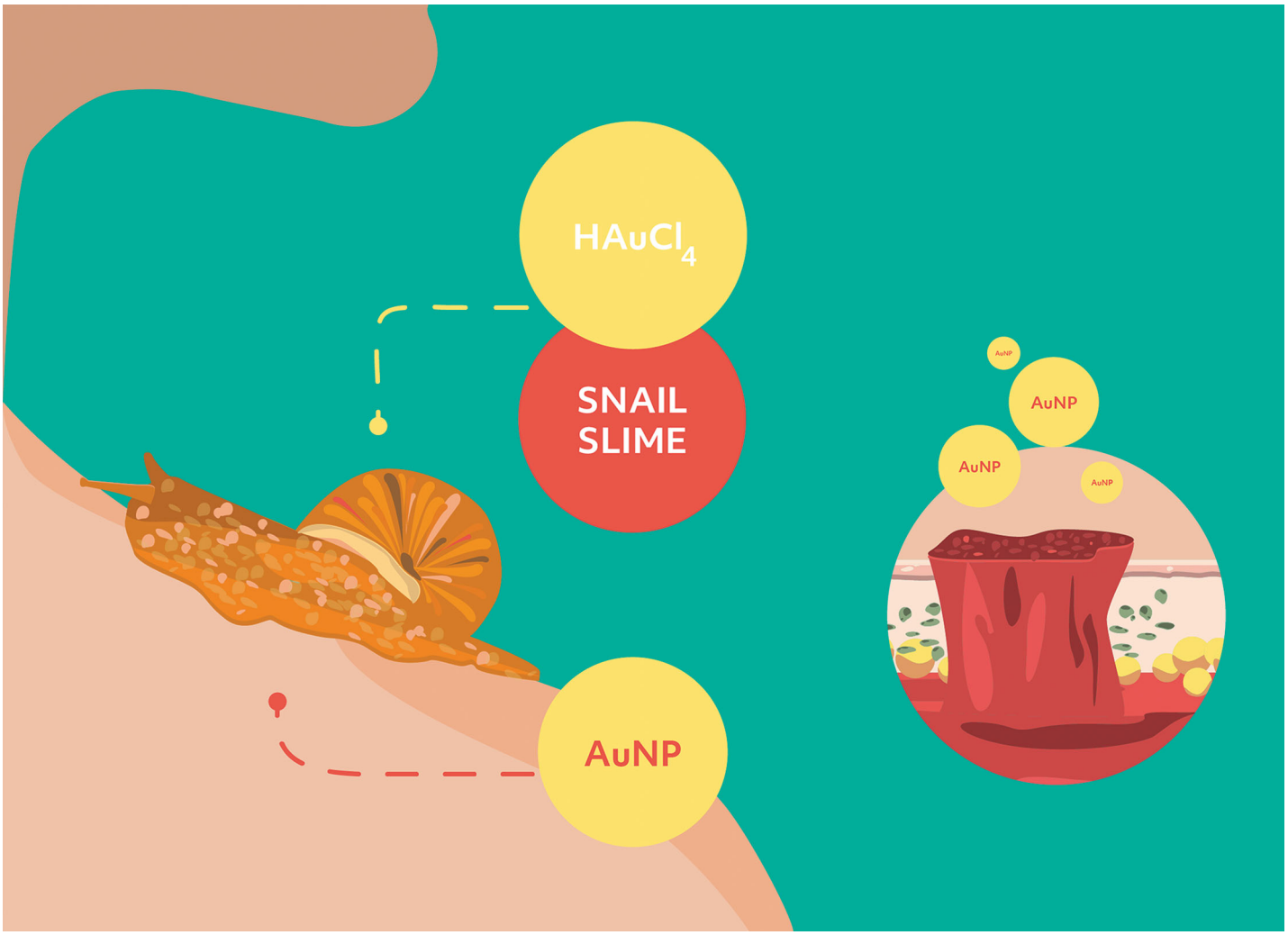

Showcasing experiments from the Department of Chemistry, University of Bari Aldo Moro, Italy.

Biomolecules from snail mucus (*Helix aspersa*) conjugated gold nanoparticles, exhibiting potential wound healing and anti-inflammatory activity

The green synthesis of gold nanoparticles by using snail slime was performed. A preliminary physico-chemical characterization was carried out. Wound healing and anti-inflammatory properties were demonstrated.

The authors would like to acknowledge Alessandra Nuzzo A\project as the artist of the cover artwork.

As featured in:

See Pinalysa Cosma *et al.*, *Soft Matter*, 2020, **16**, 10876.

ROYAL SOCIETY OF CHEMISTRY

rsc.li/soft-matter-journal

Registered charity number: 207890

Soft Matter

PAPER

View Article Online
View Journal | View Issue

Cite this: *Soft Matter*, 2020, **16**, 10876

Biomolecules from snail mucus (*Helix aspersa*) conjugated gold nanoparticles, exhibiting potential wound healing and anti-inflammatory activity†

Jennifer Gubitosa,[a] Vito Rizzi,[a] Paola Fini,[b] Anna Laurenzana,[c] Gabriella Fibbi,[c] Clara Veiga-Villauriz,[cd] Fiorenza Fanelli,[e] Francesco Fracassi,[ae] Alberto Onzo,[f] Giuliana Bianco,[f] Carmine Gaeta,[g] Antonio Guerrieri[f] and Pinalysa Cosma *[ab]

Received 11th September 2020,
Accepted 31st October 2020

DOI: 10.1039/d0sm01638a

rsc.li/soft-matter-journal

In this work, for the first time, snail slime from garden snails "*Helix Aspersa Müller*", has been used to induce the formation of eco-friendly gold nanoparticles (AuNPs-SS) suitable for biomedical applications. An AuNPs-SS comprehensive investigation was performed and AuNPs with an average particle size of 14 ± 6 nm were observed, stabilized by a slime snail-based organic layer. Indeed, as recognized in high-resolution MALDI-MS analyses, and corroborated by FESEM, UV-Vis, ATR-FTIR, and XPS results, it was possible to assess the main presence of peptides and amino acids as the main components of the slime, that, combined with the AuNPs confers on them interesting properties. More specifically, we tested, *in vitro*, the AuNPs-SS safety in human keratinocytes and their potential effect on wound healing as well as their anti-inflammatory properties in murine macrophages. Moreover, the AuNPs-SS treatment resulted in a significant increase of the urokinase-type plasminogen activator receptor (uPAR), essential for keratinocyte adhesion, spreading, and migration, together with the reduction of LPS-induced IL1-β and IL-6 cytokine levels, and completely abrogated the synthesis of inducible nitric oxide synthase (iNOS).

Introduction

The human body has different ways of protecting itself against potential injuries and infections, by means of skin characteristics acting as an effective barrier. The physiological process of tissue repair at an injured site is wound healing, which represents a complex integrated system of biological and molecular processes, such as cell migration, proliferation, extracellular matrix deposition, and remodeling.[1] Under normal conditions, the healing process cascade is initiated by an inflammatory phase resulting in granulation tissue accumulation, and scar remodeling after epithelial wound closure has been accomplished.[2] A normal wound healing process is constituted by various phases: coagulation (hemostasis), inflammation, cellular migration and proliferation, protein synthesis and wound contraction (fibroplasia), and scar formation (remodeling). Among these phases, three are the most important for successful wound healing: fibroplasia, angiogenesis, and re-epithelialization. A delay in the development of these mechanisms leads to failure or prolongs the wound healing process with a crucial part attributable to wound neovascularization.[3,4] However, any change or pathological problem (for example ischemia, diabetes mellitus, and so on) may result in the formation of chronic wounds difficult to heal, due to the failure of the normal wound healing process.[3,5] Another very important objective of wound treatment is inhibition of all the pathogenic organisms able to cause serious infection, by accelerating the healing process with cicatrices and pain reduction for patients of all ages.[5] In fact, any delay during the tissue repair process could be defined as chronic injury and can have a highly detrimental impact on human health, being more subjected to pathogens. Rapid closure of dermatological wounds is of vital importance in preventing infection and reducing

[a] *Università degli Studi "Aldo Moro" di Bari, Dip. Chimica, Via Orabona, 4 – 70126 Bari, Italy. E-mail: pinalysa.cosma@uniba.it*
[b] *Consiglio Nazionale delle Ricerche CNR-IPCF, UOS Bari, Via Orabona, 4 – 70126 Bari, Italy*
[c] *Dipartimento di Scienze Biomediche Sperimentali e Cliniche "Mario Serio" Viale Morgagni 50 – 50134, Florence, Italy*
[d] *Faculty of Medical and Human Sciences, The University of Manchester, Stopford Building, Oxford Road, Manchester M13 9PT, UK*
[e] *Consiglio Nazionale delle Ricerche, Istituto di Nanotecnologia (CNR-NANOTEC) c/o Dipartimento di Chimica, Università degli Studi "Aldo Moro", Via Orabona, 4 – 70126 Bari, Italy*
[f] *Dipartimento di Scienze, Università degli Studi della Basilicata, Via dell'Ateneo Lucano, 10 – 85100, Potenza, Italy*
[g] *Dipartimento di Chimica e Biologia, Università degli Studi di Salerno, Via Giovanni Paolo II, 132 – 84084, Fisciano, Italy*
† Electronic supplementary information (ESI) available. See DOI: 10.1039/d0sm01638a

post-treatment side-effects.[6] So, shortening the chronic wound healing process is a prime challenge in modern dermatology.[7]

Several different topical and systemic agents, together with the antimicrobial ones, have been developed for improving the cure for surgical and traumatic wounds. However, these functional topical biomaterials might delay re-epithelialization and might result in a risk of oversensitivity and resistance.[4] Hence, some alternative wound treatment methods have been searched for and, in this regard, the use of nanotechnology could be useful as a prominent scientific discipline in the technological revolution of this millennium.[8] Nanobiotechnology-based therapies in the field of wound healing are considered to be a promising area with new benefits based on the utilization of bionanomaterials in promoting wound healing, including antibacterial, anti-inflammatory, regulating extracellular matrix production, promoting stem cell proliferation and differentiation, and enhancing growth factors.[9] Many studies, involving the use of gold nanoparticles (AuNPs) with different sizes and morphologies, have been proposed in biomedical applications for skin injury therapy with great potential.[6] AuNPs have received great attention due to their low toxicity to animal and microorganism cells compared to other metal nanoparticles,[10] thus promoting their use as drug delivery systems, markers, and photothermal agents, as well as radiotherapy enhancers.[6] Recent studies have established new prospects for developing properly functionalized AuNPs for wound healing, acting as triggers to activate the proliferation and migration of wounds.[7,11,12] The AuNP use should have benefits including enhanced mechanical stability and resistance against enzymatic degradation when incorporated into tissue scaffolds, in the presence of antibodies, growth factors, and peptides, rendering them promising candidates for skin tissue engineering applications.[8]

Chemical methods, in which reduction or co-precipitation processes take place for the generation of nanoparticles, have been investigated since ancient times. However, the main drawbacks of these synthetic routes are the use of harsh chemical conditions and organic solvents, and the production of toxic by-products during the synthesis and/or functionalization of nanoparticles. For this purpose, many studies are focused on finding alternative therapeutic approaches by adopting biocompatible, safer, and greener methods employing plant extracts for fast and economical synthesis of biogenic nanogold.[13–15] Green synthesized AuNPs can also exhibit anticancer and antimicrobial activity,[16] antioxidant moisture retention, skin lightening properties,[17] and sunscreen ability, enlarging their applicability.[18,19] As reported by Gonnelli *et al.*,[20] synthetic routes relying on green chemistry show other advantages for large scale production adopting mild conditions of work.[20] For green synthesized AuNPs, additional assembling steps are not necessary since the AuNP properties are ascribed to the main components present on their surface and used to induce their formation. Thus, considering these factors, snail secretion (SS) from *Helix Aspersa*, currently revolutionizing the world of cosmetics and human skincare, has been used in this work for synthesizing AuNPs (AuNPs-SS), conferring on them interesting properties. Indeed, the SS protein content plays a key role in cell regeneration and growth, preventing the effect of inflammatory disease.[21,22] The SS main compounds are used as reducing agents enabling AuNP synthesis *via* the reduction of Au(III), from a $HAuCl_4$ solution, to Au(0), while forming an organic layer around the AuNPs. AuNPs-SS are thus synthesized by using a single step reaction, avoiding the use of additional and toxic agents. The nanoconfined main components of the SS on the AuNP surface could be an interesting way of improving the whole process, combining the properties of gold and SS. For example, Conte *et al.*[23] reported that the pharmacokinetics of snail components does not permit their optimal absorption, so the combined use of AuNPs, well-known antibacterial agents, and SS could be a functional ingredient in the treatment of acne and in biotechnology, or used as a preservative in cosmetic product formulation. Considering the overall published literature,[21,22,24–27] although interesting information can be found on the SS use, the presence of fragmentary and not detailed investigations suggests that this research field has not been extensively explored yet. In a time when cosmetic dermatology and beauty care are increasingly influential,[28,29] we intend to discuss the biogenic formation of AuNPs-SS by characterizing them and by using as accelerating wound healing and anti-inflammatory agents in biomedicine. More specifically, we tested the effect of AuNPs-SS on improving wound healing in human keratinocytes. Furthermore, considering that gold has been used historically in the treatment of painful inflammatory conditions, such as rheumatoid arthritis, and snail slime has been proved to clear up skin inflammation, we evaluated the potential anti-inflammatory properties of AuNPs-SS in murine macrophages.

Experimental

Chemicals

$HAuCl_4$ and KCl used for zeta potential measurements were purchased from Sigma-Aldrich (Milan, Italy). Snail slime was received from the Società Agricola Dap, di Francesco Paolo Perrotta & C. S.a.s – *via* Diego Rapolla – 85029 Venosa (Potenza, Basilicata, Italy). NCTC2544 human keratinocytes and RAW 264.7 macrophages were purchased from American Type Culture Collection (ATCC, Rockville, MD) and maintained at 37 °C in DMEM media (Euroclone) in a humidified 5% CO_2 incubator maintained at 37 °C (Thermo Scientific, Waltham, MA). For RAW 264.7 cells, the complete media contained L-glutamine, 100 U penicillin or streptomycin per mL, and 10% inactivated fetal calf serum (FBS, Euroclone). In the LPS stimulated macrophage experiments, RAW 264.7 cells were pre-treated overnight with 1 μg LPS per mL. The day after, LPS was removed and the cells were replaced with fresh media in the presence of AuNPs-SS.

Mechanical extraction of snail slime

The snail *Helix Aspersa Muller* is a terrestrial gastropod mollusk that in the adult phase has a shell of 3.5 cm diameter with a weight of about 15 g. Among the mechanical methods that do not damage the animal, the use of natural gas as ozone was selected to induce the production of snail slime. The mechanical extraction involved the use of equipment that within a few hours allows us to obtain the slime. More specifically, the snails were

inserted into a machine in which ozone was nebulized for about an hour; the O_3 generates a sort of excitement that induces slime production avoiding stress for the snails.

AuNPs-SS synthesis

$HAuCl_4$ was solubilized in deionized water to obtain a 1.0×10^{-3} stock solution. 1.5 mL of this solution were mixed with 2 mL of water and 500 μL of the received SS. The mixture was moderately stirred at room temperature. UV-Vis spectra of this solution were recorded soon after the preparation and at 4, 6, 24, 48, and 72 h after to monitor the AuNPs-SS formation. The induced AuNPs-SS were purified at each acquisition time, and the excess SS and the unreacted $HAuCl_4$ were removed by washing in freshwater and centrifuging (7000*g*, for 10 minutes). Before the spectra acquisition, the obtained solutions were properly diluted if necessary. It is worth mentioning that if other SS and $HAuCl_4$ amounts and ratios were explored, the formation of AuNPs-SS was not observed, or the nanoparticles appeared aggregated and more irregular.

UV-Visible measurements

Visible absorption spectra of the solutions were recorded using a Varian CARY 5 UV-Vis-NIR spectrophotometer (Varian Inc., now Agilent Technologies Inc., Santa Clara, CA, USA) in the range 200–800 nm. The measurements were performed using a cuvette with 1 cm path length.

ATR-FTIR spectroscopic measurements

ATR-FTIR spectra were recorded in a 600–4000 cm^{-1} range, at a resolution of 4 cm^{-1}, using a Fourier Transform Infrared spectrometer 670-IR equipped with an ATR device (Varian Inc., now Agilent Technologies Inc., Santa Clara, CA, USA). 32 scans were summed for each acquisition.

Field emission scanning electron microscopy (FESEM)

A Zeiss SUPRA™ 40 field emission scanning electron microscope was used for the morphological investigation of the AuNPs-SS. FESEM images were acquired using a high resolution in-lens secondary electron detector at an electron acceleration voltage (extra-high tension, EHT) of 20 kV, a working distance of 4 mm, and magnification in the range 100–1000k×. The size distribution of the AuNPs as well as the thickness of the organic layer covering the AuNPs was estimated by FESEM. For FESEM and XPS investigation, AuNPs-SS were dispersed in water, deposited by drop-casting onto the small pieces of Si(100) wafer, and analyzed after solvent evaporation at room temperature.

X-Ray photoelectron spectroscopy (XPS)

XPS analyses were performed using a PHI VersaProbe II spectrometer equipped with a monochromatic Al Kα X-ray source (1486.6 eV) operated at a spot size of 100 μm corresponding to a power of 24.5 W. Survey (0–1400 eV) and high resolution (C 1s, O 1s, N 1s, Au 4f) spectra were recorded in FAT (fixed analyzer transmission) mode at a pass energy of 117.4 and 46.95 eV, respectively. All spectra were acquired at a take-off angle of 45° with respect to the sample normal. Dual-beam charge neutralization was constantly applied during the analysis. XPS analysis was repeated on three different spots of the sample. Special attention was devoted to verifying that no change in the sample was induced upon exposure to the X-ray beam and to the dual-beam used for charge neutralization. Detailed spectra processing was performed using commercial MultiPak software (Version 9.5.0.8, 30-10-2013, Ulvac-PHI, Inc.). Charge correction of the spectra was performed by taking the hydrocarbon (C–C/C–H) component of the C 1s spectrum as an internal reference (binding energy, BE = 285.0 eV). The high-resolution spectra were fitted with mixed Gaussian–Lorentzian peaks after a Shirley background subtraction. A maximum relative standard deviation of 10% was estimated on the area percentages of the curve-fitting components, while the determined standard deviation of their position was ±0.2 eV.

Zeta potential and size measurements

The average of the hydrodynamic diameters and the polydispersity index (PDI) of the AuNPs-SS were measured by dynamic light scattering and using a Zetasizer Nano ZS (Malvern Instruments Ltd, Worcestershire, UK). The surface charge of AuNPs-SS was measured as zeta potential by laser Doppler velocimetry using the same instrument after dilution with 1 mM KCl.

Mass spectrometry analysis

High-resolution mass spectra were acquired on a Bruker (Bruker Daltonik GmbH, Bremen, Germany) solariX XR Fourier transform ion cyclotron resonance mass spectrometer (FT-ICR-MS) equipped with a 7 T superconducting magnet and a MALDI source. The spectra were acquired with a time domain size of 16 mega-word, an accumulation time of 0.1 s, and a mass range of 100–2000 *m*/*z*. Moreover, the average number of scans was set to 50. For the analysis, a laser power of 32% and a number of laser shots of 28 were assumed. 2,5-Dihydroxybenzoic acid was used as a matrix, while a solution of this compound and pure snail slime (or AuNP slime sample), in a 1 : 1 ratio, was prepared and analyzed. The mass measurement accuracy reached values of less than 0.1 ppm.

Cell viability determination

The viability of NCTC2544 human keratinocyte and RAW 264.7 macrophages was determined by trypan blue staining. NCTC2544 cells (2.0×10^5) were seeded in 6-well plates and allowed to attach overnight. On the next day, AuNP colloidal solutions were added at the indicated concentrations. 48 h later, 20 μL of cells were aseptically transferred to a 1.5 mL clear Eppendorf tube and incubated for 3 min at room temperature with an equal volume of 0.4% (w/v) trypan blue solution prepared in 0.81% NaCl and 0.06% (w/v) dibasic potassium phosphate. Viable and nonviable cells (trypan blue positive) were counted separately using a dual-chamber hemocytometer and a light microscope. RAW 264.7 cells (3.0×10^5) were seeded in 6-well plates and allowed to attach overnight. On the next day, the cells were pre-treated overnight with 1 μg LPS per mL. The day after the LPS was removed and the cells were replaced with fresh media in the presence of AuNPs-SS. 24 h later, the viable and non-viable cells were

counted as described for NCTC2544. The means of three independent cell counts were pooled for analysis.

Scratch assay

The migratory potential of the keratinocyte cell line NCTC2544 was assessed with a wound healing scratch assay.[30] NCTC cells were grown to confluence in 60 mm culture plates at a concentration of 2×10^5 cells in complete media. A straight scratch was made in the confluent monolayer with a p200 pipet tip. The detached cells were removed, and the edge of the scratch was flattened by washing the cells twice with PBS. The cells were replaced with complete media and treated with increasing concentrations of AuNPs-SS to monitor cell motility. The scratched areas for each sample were marked and photographed immediately and after 24 and 48 hours with an EVO digital camera (Coolpix 5400, Nikon Corporation, Japan). Using the ImageJ image processing program, the size of the denuded area was determined at each time point from the digital images. The migrated area was calculated by subtracting the wound area at time point t = 24 hours and t = 48 hours from t = 0 h.

RNA extraction and semiquantitative and quantitative PCR

Total RNA was prepared using Tri reagent (Sigma-Aldrich, Saint Louis, Missouri, USA), agarose gel was checked for integrity, and reverse transcribed with a cDNA synthesis kit (BioRad, Milano, Italy) according to manufacturer's instructions. The selected genes were evaluated by qualitative PCR using Blue Platinum PCR Super Mix (Life Technologies, Monza, Italy). The primer sequences (IDT, TemaRicerca, Bologna, Italy) were as follows:

IL1-β Forward 5′-CCTGCAGCTGGAGAGTGTGGA-3′; Reverse 5′-AGGAGGAACGGA-GACTACCC-3′

iNOS Forward 5′-CCC TTC CGA AGT TTC TGG CAG CAG C-3′; Reverse 5′-GGC TGT CAG AGC CTC GTG GCT TTG-3′

IL6 Forward 5′-CGG AGA GGA GAC TTC ACA CAG GA-3′ Reverse 5′-GGA GAG CAT TGG AAA TTG GGG-3′

β-actin Forward 5′ GGC ACC ACA CCT TCT ACA ATG-3′ Reverse 5′-GGG GTG TTG AAG GTC TCA AAC-3′

Western blot analysis

The harvested cells were resuspended in 20 mM RIPA buffer (pH 7.4) (Merk Millipore, Vimodrone, MI, Italy) containing a cocktail of proteinase inhibitors (Calbiochem, Merck, Darmstadt, Germany) and treated by sonication (Microson XL-2000, Minisonix, Farmingdale, NY, USA). Aliquots of supernatants containing equal amounts of protein (30 μg) in Laemmli buffer were separated on Bolt® Bis-Tris Plus gels with 4–12% precast polyacrylamide gels (Life Technologies, Monza, Italy) and then transferred from the gel to a PVDF nitrocellulose membrane using an iBlot 2 system (Life Technologies, Monza, Italy). The blots were stained with Ponceau red to ensure equal loading and complete transfer of proteins. Then, they were blocked for 1 hour, at room temperature, with 5% milk in PBS 0.1% and tween solution. Subsequently, the membranes were probed at 4 °C overnight with the following primary antibodies: rabbit anti-uPAR (1 : 500 FL 290, Santa Cruz Biotechnology, Cat# sc-10815); rabbit anti-iNOS (1 : 1000, Cell signaling, Cat#2982) and rabbit GAPDH antibody (1 : 1000, Cell signaling Technology, Cat# 2118) were used to assess equal amounts of protein loaded in each lane. Anti-rabbit IgG (whole molecule)–peroxidase antibody (Sigma, Cat#A0545) was used as the secondary antibody; the ECL procedure was employed for development.

Results and discussion

After mixing, under continuous stirring, appropriate amounts of SS and $HAuCl_4$, the formation of AuNPs-SS was observed. More specifically, by diluting the received SS in a dilution factor of 1 : 8, fixing the $HAuCl_4$ concentration at 4.0×10^{-4} M, the reaction mixture color changed from light yellow, soon after the preparation (Fig. 1A, picture 1), to dark purple (Fig. 1A, picture 2) extending the reaction time to 48 h, thus indicating the AuNPs-SS formation. Along with scattering effects, the color of colloidal gold is due to the surface plasmon resonance (SPR) phenomenon, a characteristic signal in the visible absorption spectrum of AuNPs. In general, this signal is located in the range from 500 to 600 nm of the UV-Vis region of the electromagnetic spectrum. In this case, the mixture of $HAuCl_4$ and SS presents a AuNP characteristic SPR band, which appeared slightly broadened and centered at 550 nm (Fig. 1B). In particular, as shown in Fig. 1B, the AuNP SPR band time evolution is reported, while in Fig. 1C and D, the wavelength and absorption values at the maximum of SPR are shown as a function of time compared with the full width at half maximum (FWHM). A shift towards higher wavelength number values, along with an increase of A_{max}, was observed upon extending the reaction time. At the same time, the corresponding FWHM became larger than the values observed at the beginning of the reaction (Fig. 1C and D). According to Yin *et al.*,[31] the changes, in terms of form and width, in the SPR bands can always be attributed to a different distribution of the nanoparticles in solution and their aggregation. Moreover, the SPR absorption intensity of AuNPs depends on their size and shape as well as their surrounding medium.[31]

Therefore, in agreement with the SPR band position and shape, the spectral observations indicated polydispersed AuNPs that tend to slightly increase in their size with the elapsed reaction time. Probably, the observed increment in A_{max}, passing from 4 to 48 h, could be attributed to an increase in the AuNPs-SS concentration due to the quite complete reaction of $HAuCl_4$ with SS. Further, it is worth mentioning that, with the increasing reaction time until 72 h, the particles tended to aggregate to each other and the SPR signal decreased, becoming barely evident in the UV-Vis spectrum (data not shown).

As a whole, the results indicated the reduction of Au(III) to Au(0), forming nanoparticles thanks to the synergistic action, as reducing agents, of the main components of snail mucus. Indeed, the chemical reduction of $HAuCl_4$ aqueous solution is one of the most widely used methods for the synthesis of colloidal gold.[32] Not surprisingly, by looking at the AuNPs-SS spectrum shape line, in particular below 400 nm, the contribution of chemical species, like proteins/peptides and amino acids, mainly present in SS,[33] absorbing in this region, was observed.

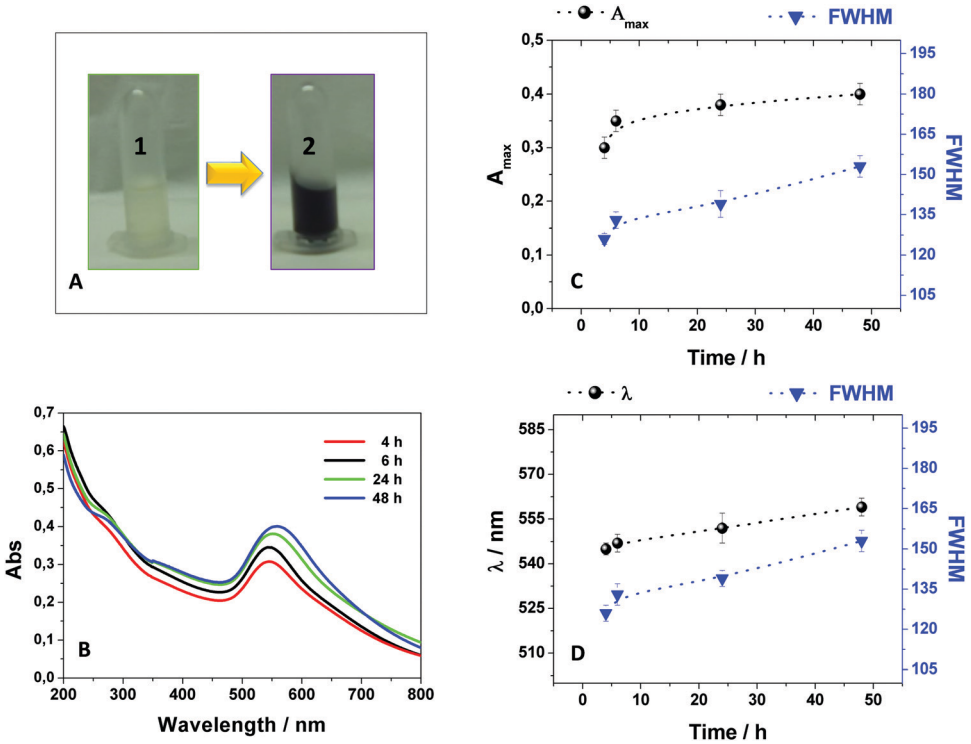

Fig. 1 Camera pictures of a $HAuCl_4$ solution at 4.0×10^{-4} M in the absence (1) and presence (2) of SS (A); UV-Vis spectra of solutions containing AuNPs (diluted 1 : 5), showing the typical SPR, collected at different incubation times from the mixture of $HAuCl_4$ and SS (B); time evolution of SPR absorbance intensity (A_{max}) *versus* the related FWHM (C); time evolution of the SPR wavelength registered in accordance with the A_{max} *versus* the SPR FWHM (D).

The finding was confirmed by comparing the UV-Vis spectrum of SS solutions with the AuNP spectrum (Fig. S1, ESI†). The UV-Vis spectra of SS collected at different dilutions (to get better evidence of the contribution of the absorbance values in the reported wavelength region) clearly displayed the contribution of the main SS components, indicated with arrows, on the AuNP surface.

A zeta potential value of approximately -35 ± 2 mV was measured for AuNPs-SS, indicating their good stability in water. Further, Fig. S2 (ESI†) shows a comparison between the UV-Vis spectra of AuNPs-SS collected soon after the synthesis (selecting 24 h as the reaction time) and after 2 months. It is clearly evident that the AuNPs-SS are characterized by long-term stability, as indicated by the presence of the AuNP SRP signal.

FESEM analysis

FESEM investigation revealed the formation of irregularly shaped AuNPs (Fig. 2A and B), with a minimum and maximum size of about 4 and 50 nm, respectively, and an average size of 14 ± 6 nm (particle size distribution in Fig. 2C). The FESEM images confirmed the hybrid organic–inorganic nature of the AuNPs-SS and, in particular, evidenced the presence of a thin organic layer covering the Au nanoparticles (thickness ranging between 4 and 8 nm, Fig. 2B).

So, starting from these considerations and considering an AuNPs-SS average size of 14 ± 6 nm, a molar absorption coefficient of 3.7×10^8 M^{-1} cm^{-1} was calculated. As a result, each synthesis produced, adopting 24 h as the reaction time,

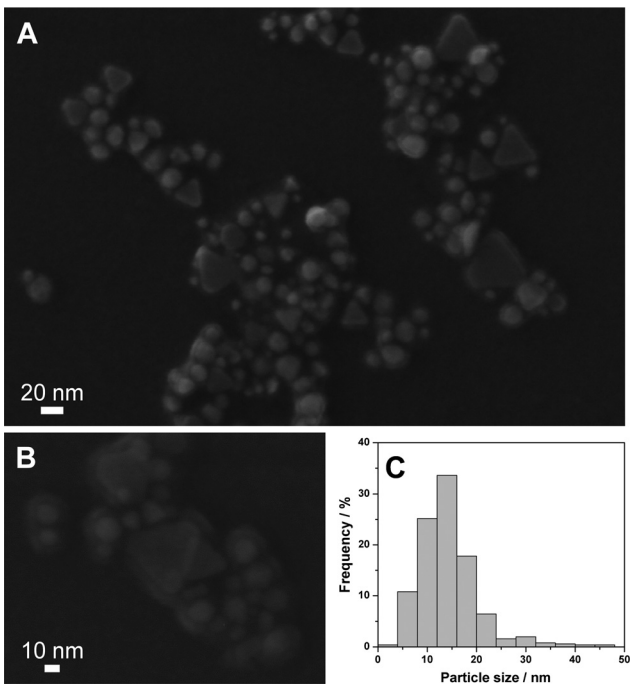

Fig. 2 FESEM images of AuNPs-SS (A and B); AuNP size distribution determined from FESEM images (500 particles) (C).

AuNPs-SS stock solutions with a mean concentration of 5×10^{-9} M; this means 1.64×10^{12} AuNPs per mL. Further, in order to evaluate the yield of the reaction, the synthesized AuNPs

were isolated, dried in an oven at 50 °C and weighed. 1.0 ± 0.2 mg mL^{-1} of AuNPs-SS were obtained, under the proposed conditions of work. The percentage of reacted Au(III) was also theoretically calculated by considering the following assumptions: (i) the starting concentration of $HAuCl_4$ was 4.0×10^{-4} M corresponding to 0.08 mg of Au(III), (ii) the AuNPs were assumed to have a spherical shape with a diameter of 14 nm (Fig. 2C), and (iii) the density of Au(0) in the AuNP core was 19.32 g cm^{-3}. So, by considering the volume of a sphere $\left(\frac{4}{3}\pi r^3\right)$ and 1.64×10^{12} AuNPs per mL, the results indicated that the proposed synthesis afforded a reaction yield of about 62.5%.

XPS analysis

XPS results showed that the surface atomic concentrations of carbon, oxygen, nitrogen, and gold are about 64, 18, 11, and 7%, respectively (XPS survey spectrum in Fig. S3, ESI†). Fig. 3A reports the high-resolution Au 4f XPS spectrum consisting of a doublet (*i.e.*, Au $4f_{7/2}$ and Au $4f_{5/2}$ at 83.2 and 86.9 eV, respectively) due to spin–orbit coupling, the position being in agreement with the literature on AuNPs.[18,34–37] The curve fitting of the Au 4f signal indicates three Au $4f_{7/2}$ components, *i.e.*, the main component at 83.2 eV (68%) attributed to metallic gold (Au(0)), and the minor peaks at about 84.2 eV (23%) and 85.4 eV (9%) ascribed to Au(I) and Au(III), respectively (the total area of Au $4f_{7/2}$ is taken as 100%).[37–40] The high-resolution C 1s XPS spectrum in Fig. 3B is curve-fitted with four peaks and, specifically, the hydrocarbon component at 285 eV (51%) and the component at 286.4 eV (31%) are ascribed to both C–N and C–O groups; the peak at 288.0 eV (14.5%) is assigned to both C═O and O–C–O moieties and the weak peak at 289.2 eV (3.5%) is due to carboxylic functionalities. The O 1s spectrum in Fig. 3C displays two components, *i.e.*, the peak at 531.7 eV (57%) that can be ascribed to the O═C moieties and the component at 533.1 eV (43%) associated with O–C groups. The N 1s signal (Fig. 3D) shows one main peak at about 400.1 eV, consistent with the presence of amine and amide groups.[41–43] To unveil the nature of these compounds on the AuNP surface, ATR-FTIR and MALDI-MS analyses were performed.

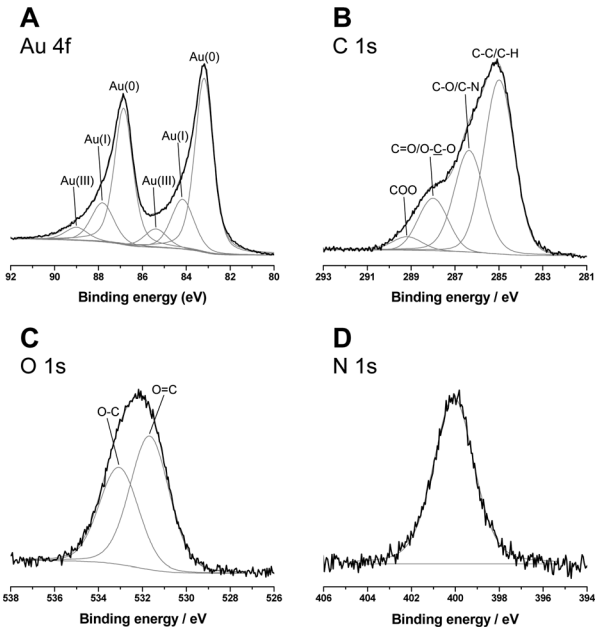

Fig. 3 High resolution XPS spectra of the AuNPs-SS and their relative curve-fitting: Au 4f (A), C 1s (B), O 1s (C), and N 1s spectra (D).

ATR-FTIR spectroscopic measurements

FTIR measurements were carried out to recognize the possible functional groups responsible for the efficient stabilization of gold nanoparticles prepared by using SS. For this purpose, a comparison between the ATR-FTIR spectra of SS before and after the formation of AuNPs and the FTIR spectrum of AuNPs-SS was drawn (Fig. 4).

Starting from the as received SS, bands around 1700 cm^{-1} and 1580 cm^{-1} were detected, and in accordance with the literature,[33,44,45] these peaks indicated the main presence of amide bonds of peptides and proteins as glycosaminoglycans and proteoglycans. Further, the bands at about 1388 cm^{-1} and 1700 cm^{-1} could suggest the presence of carboxylate moieties associated with the acid derivatives of sugars and amino acid chains. Indeed, the peaks at 1192 cm^{-1} and the lower wavenumber values (below 900 cm^{-1}) indicated *O*-glycosidic linkages.[33] In this region, the contribution of sulphonated, acylated, and ester-based compounds should be also considered. The shoulder at 1360 cm^{-1} with a partial contribution at 1380 cm^{-1} indicated the presence of carbon chains of proteins and carbohydrates.[33,44,45] Accordingly, there was evidence at 2850 cm^{-1} and 2930 cm^{-1} of CH_2, and CH_3 arises from the protein skeleton and lipidic component of the slime.[30] The observed bands between 2900 and 3500 cm^{-1} can be ascribed to the presence of a large amount of OH and NH moieties. The contributions of polyphenols, mainly in the range of 1500–3500 cm^{-1}, cannot be excluded.[18] Overtones of the benzene rings of phenylaniline and tyrosine were detected above 1800 cm^{-1} and 2600 cm^{-1}.[33] Interestingly, after the contact with $HAuCl_4$ solution, and thus after the AuNP formation, the SS

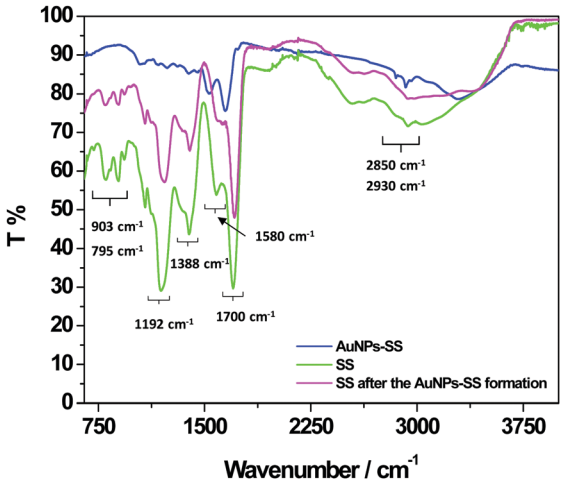

Fig. 4 ATR-FTIR spectra of SS, AuNPs-SS and SS after the AuNP formation.

spectrum appeared almost unchanged as a whole in comparison with the one observed at the beginning of the reaction. In particular, the signal at 1580 cm^{-1} decreased in its intensity, but the other main vibrations at 1700 cm^{-1} and 1192 cm^{-1} were retained. On the one hand, the change of the amide bond signals from peptides and protein features was indicative of their role in the formation of AuNPs-SS, and on the other hand, the counterpart of the spectrum ascribed to the sugar derivatives did not show important modifications. The wavenumber region 2800–3500 cm^{-1} also seemed affected, suggesting the contribution of biomolecules having OH and NH functionalities. These results were confirmed when the FTIR-ATR result of the AuNPs-SS was collected. Indeed, the main signals at 1645 and 1545 cm^{-1} indicated the presence of a protein component based on the amide I (C═O stretching) (1645 cm^{-1}) and II (1545 cm^{-1}) (N–H bending and C–N stretching) bands.[44] Interestingly, if these bands were compared with the signals of SS and ascribed to the same vibration modes, the observed shift towards the lower wavenumber values could be attributed to their coordination on the AuNP surface. A characteristic absorption in the region 1200–1300 cm^{-1}, which represented amide III, due to the C–N stretching and the N–H deformation bands, was also detected. Accordingly, the signals between 3300 and 3750 cm^{-1} arise also from the AuNPs-SS surface due to the N–H amine group stretching vibrations superimposed on the side of the O–H hydroxyl group stretching bands.[46] Once again, comparing the position of these bands with those observed in the as-received SS, a clear shift towards higher wavenumbers was observed confirming that the molecules in the SS could coordinate to AuNPs through the formation of Au–N or Au–O covalent bonds. In the spectral region from 750 to 1400 cm^{-1} only very weak signals can be observed. The presence of weak and minor signals at 1192, 1388 cm^{-1} and 1700 cm^{-1} should suggest the minor contribution of *O*-glycosidic linkages and carboxylate moieties associated with the acid derivatives of sugars and amino acid chains. The signal at 2850 cm^{-1} and 2930 cm^{-1} observed in the ATR-FTIR of AuNPs-SS could confirm the presence of the protein skeleton. So, from the ATR-FTIR analyses it has been possible to assess the main presence of peptides and aminoacids on the surface of AuNPs-SS, acting as reductant agents during the formation of AuNPs.

MALDI(+) FT-ICR MS analysis

The presence of amino acids and peptides was supported by MALDI(+) FT-ICR MS experiments (Fig. 5).

The MALDI(+) FT-ICR MS spectrum for the as received SS sample (Fig. 5A) shows a huge number of MS signals, thus revealing the complexity of the sample in terms of its metabolic profile. Thanks to the higher levels of accuracies achieved by the HRMS technique,[47] it was possible to unequivocally identify several protonated amino acids, *i.e.* threonine ($[C_4H_{10}NO_3]^+$, *m*/*z* 120.12747), tryptophan ($[C_{11}H_{13}N_2O_2]^+$, *m*/*z* 205.23364), arginine ($[C_6H_{15}N_4O_2]^+$, *m*/*z* 175.20953), histidine ($[C_6H_{10}N_3O_2]^+$, *m*/*z* 156.16258), asparagine ($[C_4H_9N_2O_3]^+$, *m*/*z* 133.12607), cysteine ($[C_3H_8NO_2S]^+$, *m*/*z* 122.16670), glutamine ($[C_5H_{11}N_2O_3]^+$, *m*/*z* 147.15341), proline ($[C_5H_{10}NO_2]^+$, *m*/*z* 116.13903) and serine ($[C_3H_7NO_3]^+$, *m*/*z* 106.10083), already found in the snail slime sample.[48] 6198 peptides could be identified showing the presence of at least one unit of cysteine. So, the presence of peptides, showing high contents of cysteine, proline, serine, and glycine, was also observed. It should be remembered that these compounds are very well-known in the literature for their high antimicrobial activity.[48] Instead, the analysis of the AuNPs-SS sample (Fig. 5B) shows a very different situation. In this case, the MALDI(+) FT-ICR MS spectrum of the sample shows a lower number of MS signals in comparison to the pure sample (3158 and 209 694 signals, respectively). No free amino acids were found and only 3 free peptides could be identified, thus suggesting drastic shrinkage of the range of free peptides present in the sample, indicative of their role in the formation of AuNPs.

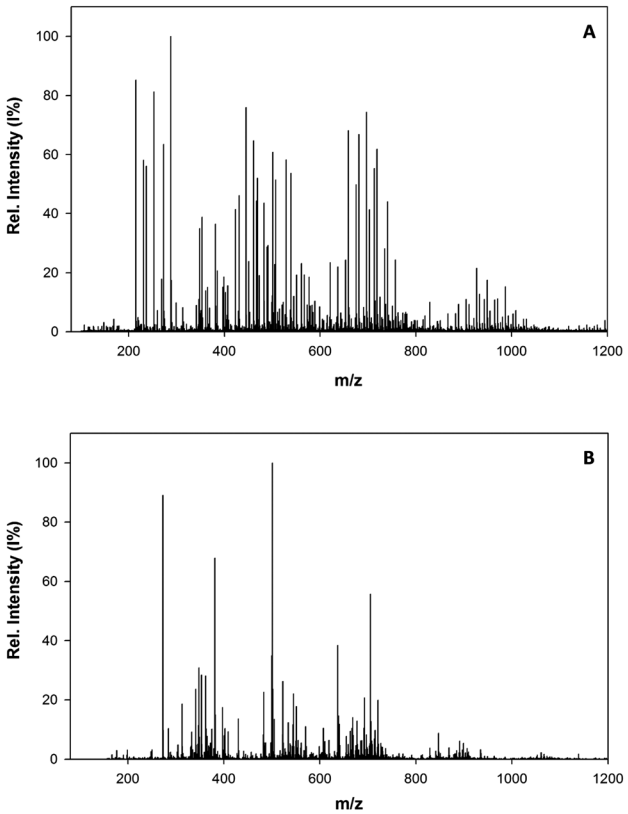

Fig. 5 Positive ion MALDI-FT-ICR MS of the snail slime (A) and AuNP snail slime (B) samples with DHB as the matrix.

The pH effect on the synthesized AuNPs

The AuNP stability, after their synthesis, was investigated under different pH values ranging from 2 to 12. Once again, by observing the SPR of the AuNPs, the wavelength and FWHM were monitored. The results, reported in Fig. 6A, indicated that both the position and the FWHM were stable in the pH range from 4 to 10 and slight changes were detected at the lowest and the highest investigated pH values, *i.e.* pH 2 and 12. More specifically, at pH 2 the SPR signal shifts towards higher wavelength values indicating the contribution of larger AuNPs that under this condition tend to agglomerate.[31] Yin *et al.*[31] suggested that a large number of H^+ ions in aqueous solution could be adsorbed onto the surface of the AuNPs, modifying their surface and charges. Accordingly, at the same time, the FWHM

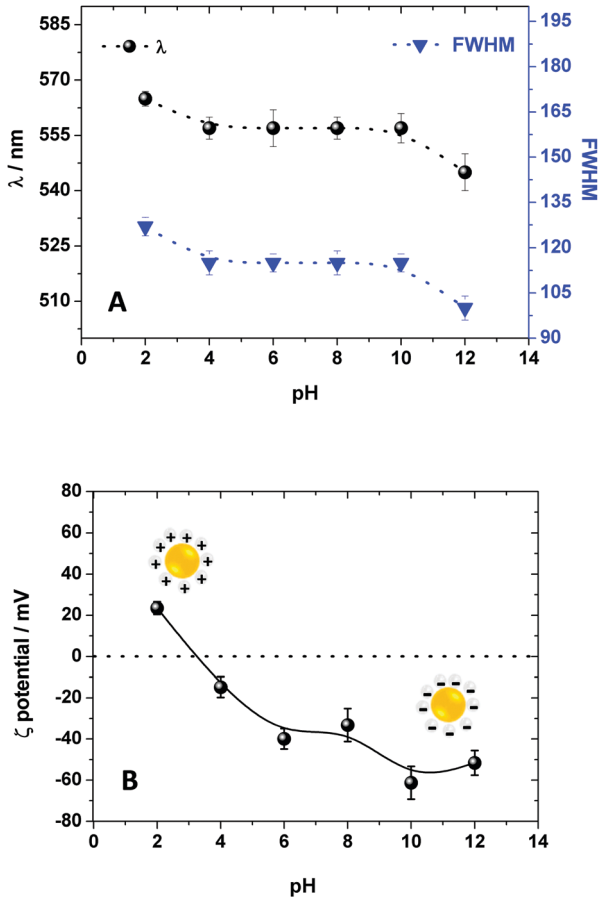

Fig. 6 Effect of pH on the SPR wavelength position and FWHM (A) and on the ζ-potential values (B).

increased. Then, the AuNPs tended to agglomerate easily and consequently, the final particle size was larger. Conversely, at pH 12, the FWHM of the AuNPs decreased in its value, indicating that the particles were more monodisperse. These findings were confirmed by performing zeta potential measurements as a function of pH values, as reported in Fig. 6B. It is worth mentioning that the zeta potential gives information about the AuNP suspension stability, since a higher electric surface charge of the AuNPs prevents aggregation. Indeed, the AuNPs were negatively charged in the range of pH from 4 to 12 and, in particular, the charge decreased with the increasing pH value. On the other hand, at pH 2 a positive zeta potential value, of approximately +25 mV, was observed, affecting the AuNP surface as previously described. The presence of functional groups arising from the main components of SS, mainly the carboxylic moieties of proteins and aminoacids (and/or polyphenols) present on the AuNP surface, produced a negative electrical charge and an observed dependence on the pH. At pH values below 4, the organic moieties were in the protonated form and the AuNPs slightly aggregated.

AuNPs-SS enhance scratch wound closure of NCTC 2544 keratinocytes

To determine whether AuNPs-SS could affect cell motility, scratch assays were performed in a confluent monolayer of keratinocytes and evaluated at 0 h, 24 h, and 48 h after treatment with increasing doses of AuNPs-SS. By 24 h, even though the keratinocytes normally showed an active migratory phenotype, scratches treated with AuNPs-SS displayed a significant acceleration of wound closure as compared with the untreated (CTRL) wound (Fig. 7A and B). By 48 h, the scratch treated with the highest AuNP dose was completely closed, thus showing a significant increase in the closure rate from 24 h, while no statistically significant change in cell viability was observed on AuNPs-SS treatment as shown in Fig. 7C. Moreover, western blot analysis displayed that AuNPs-SS treatment induced a significant increase of the urokinase-type plasminogen activator receptor (uPAR), which is essential for keratinocyte adhesion, spreading, and migration *in vitro* and *in vivo* (Fig. 8C).[49,50]

AuNPs-SS reduce the inflammatory response of LPS-activated macrophages

To further assess the possible effects of the AuNPs-SS on the biological inflammatory response, RAW 264.7 macrophages were pre-treated with LPS and the day after loading with two doses of AuNPs-SS. Morphological changes and the inflammatory gene panel were evaluated at the end of the sequential treatments. As shown in Fig. 8A, the mouse macrophage cells took up AuNP regardless of the treatment with LPS. The cells without LPS treatment were more homogeneous in size, and the AuNPs appeared to be dispersed throughout the cytoplasm. After LPS treatment, the macrophages became activated as seen by variations in size. The higher the AuNP concentration, the more activated the cells appeared, presenting extended pseudopods. It was found that there was no statistically significant change in macrophage viability (Fig. 8B). The gene expression of cytokines IL1-β and IL-6 and inducible nitric oxide synthase (iNOS) showed that in the absence of LPS treatment, there were moderate changes in cytokine expression after AuNPs-SS treatment. LPS induced a massive increase in the cytokine and iNOS expression. Interestingly, the AuNPs-SS synergistically reduced these elevated cytokine levels and completely abrogated the synthesis of iNOS (Fig. 8C). The effect of AuNPs-SS on the iNOS levels before and after LPS stimulation was confirmed also by western blot analysis (Fig. 8D). Altogether these results suggest that AuNPss-SS may have modulatory effects that could be beneficial in reducing inflammatory or pathogenic responses.

Conclusions

For the first time, in this work, snail slime was used to induce the formation of AuNPs, proposing in the literature a novel and green approach for their synthesis. A comprehensive investigation was performed in our laboratory by adopting several complementary techniques such as UV-Vis and ATR-FTIR spectroscopy and DLS, XPS, and high-resolution MALDI-MS analyses. AuNPs that are 14 ± 6 wide were observed through the FESEM investigation which evidenced the formation of the organic layer snail slime-based surrounding AuNPs. The latter was confirmed by ATR-FTIR, XPS, and MALDI-MS analyses.

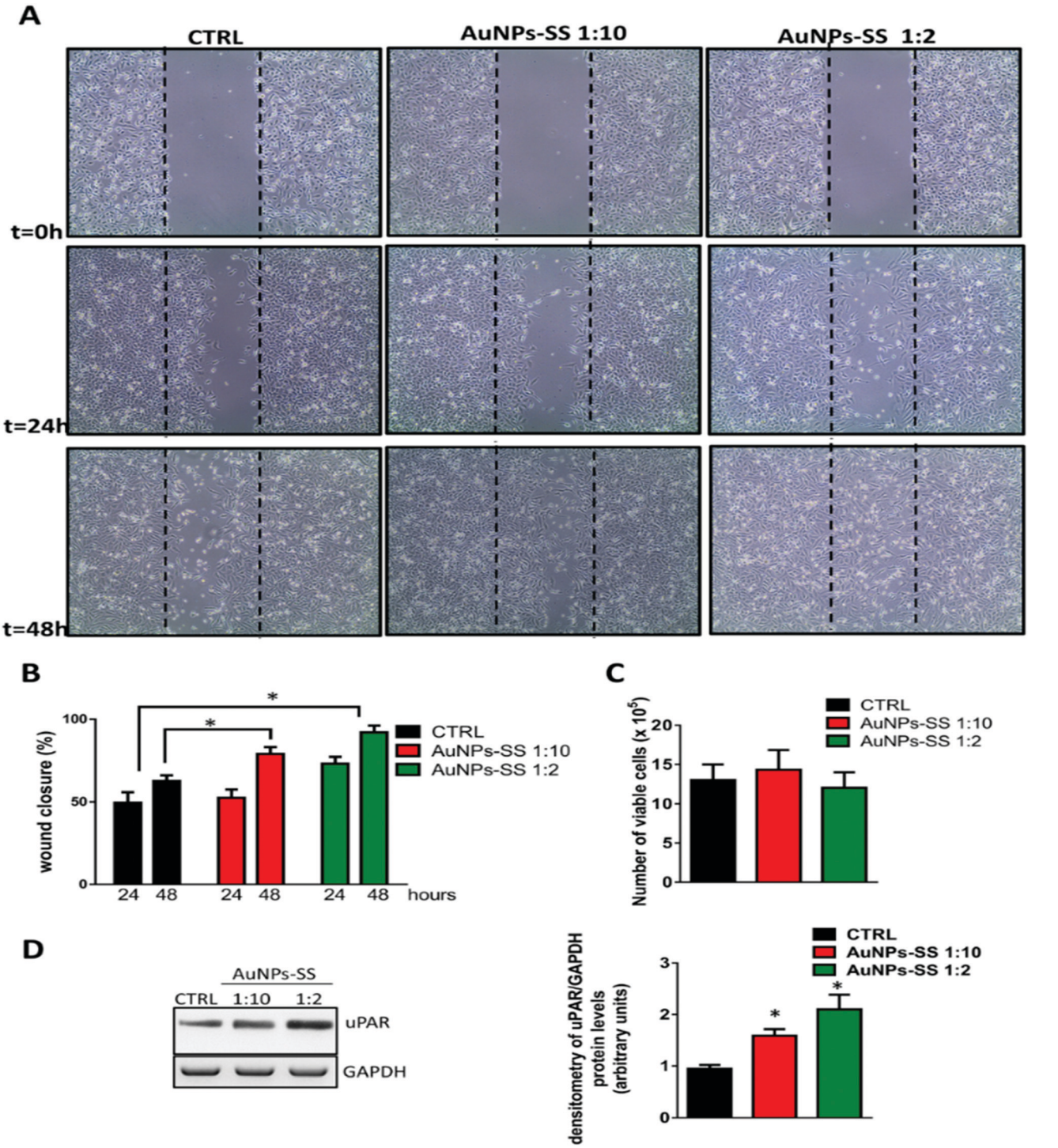

Fig. 7 Confluent monolayers of NCTC2544 were wounded by manually scratching as described in Materials and methods and incubated with increasing concentrations of AuNPs-SS. Representative pictures of the wound gap taken at 0 h, 24 h and 48 h (A); histograms show the percentage of gap closure compared with time 0 h (B); histogram representing viable cells (trypan blue negative) counted with the aid of a Burker chamber, as described in M&M (C); western blot analysis of uPAR levels quantified by densitometric analysis; GAPDH was also examined to ensure equal loading of samples in each lane. For all the panels in the figure, data in the graphs represent the mean ± SD of at least three independent triplicate experiments. Asterisks (*$p < 0.05$) indicate significant differences of AuNPs-SS treated cells, from CTRL (untreated) (D).

Indeed, the main presence of peptides and amino acids was observed at the surface of the AuNPs endowing them with a high zeta potential value in water (-35 ± 2 mV), indicative of their great stability. Indeed, the temporal and pH stability of the proposed colloidal gold solution was investigated, which resulted in a suspension that was stable for a long time and

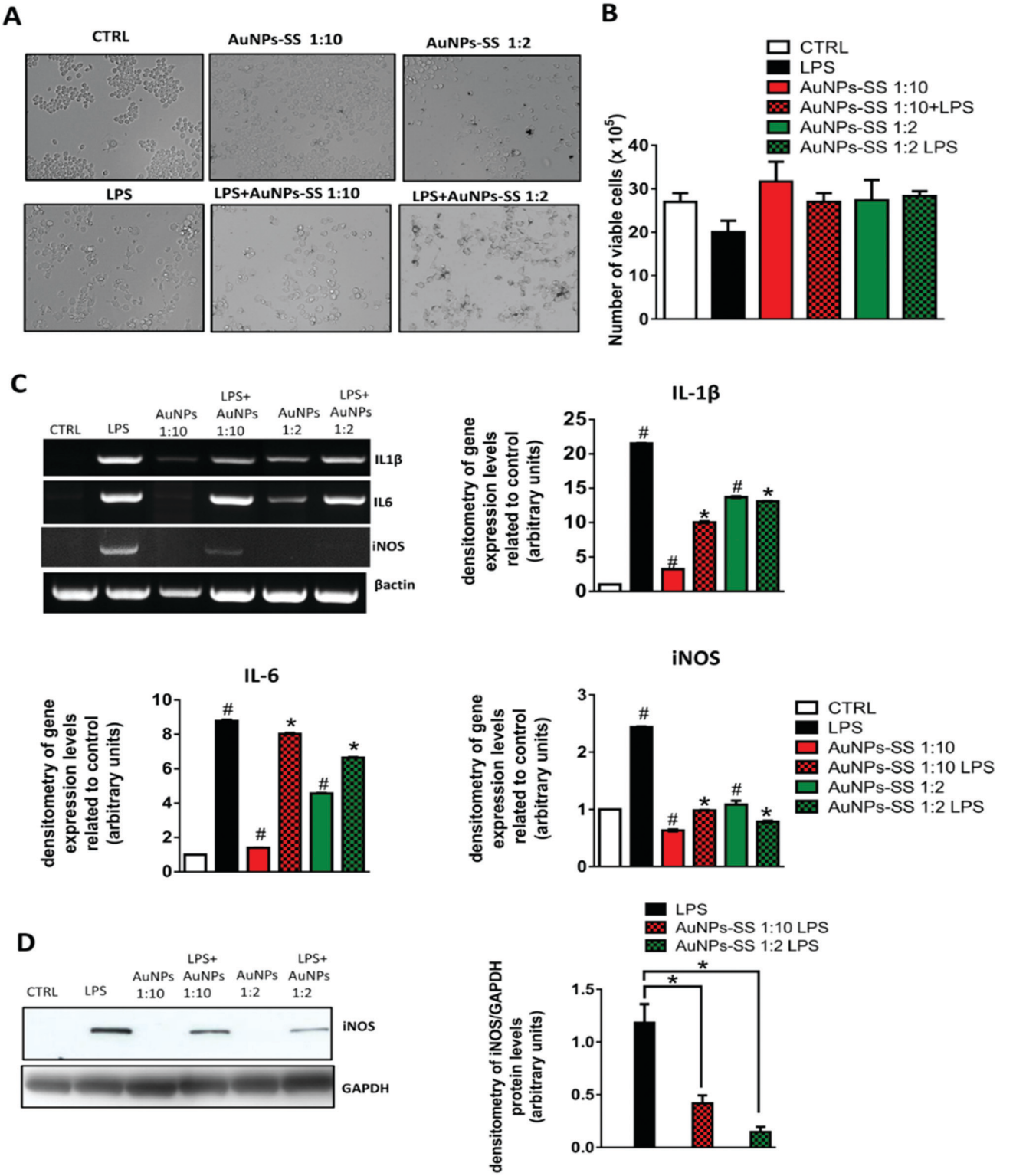

Fig. 8 Optical images of untreated, LPS treated, or AuNPs-SS treated cells (A); histogram representing viable cells (B); RT-PCR analysis of the mRNA levels of IL1β, IL6, and iNOS in cells treated as in (A) and (C). Amplification of cDNA was carried out for 30 cycles and β-actin was used as the reference gene; results were from a typical experiment out of three. Densitometric analysis of the expression gene levels is reported at the bottom. Significance was assessed by a one-way ANOVA test followed by a Newman-Keuls post test. Error bars indicate mean ± SD; asterisks (*$p < 0.05$) indicate significant differences of LPS + AuNPs-SS treated cells from LPS, while the number sign (#$p < 0.05$) indicates significant differences from CTRL (D) western blot analysis of iNOS and p65. Histograms on the right represent densitometric analysis of the iNOS and p65 protein levels. Asterisks (*$p < 0.05$) indicate significant differences of LPS + AuNPs-SS treated cells from LPS. Results were from a typical experiment out of three.

appeared only slightly affected under a high acidic pH value (pH 2), far from biological conditions, in which aggregation of AuNPs was observed. With the prospect of using the AuNPs for biomedical devices, we studied the effect of AuNPs on wound healing in human keratinocytes and evaluated their potential anti-inflammatory properties in murine macrophages. Our findings demonstrated that the accelerated wound closure promoted by AuNPs-SS was associated with an increased expression of the receptor for urokinase (uPAR) which, besides the canonical conversion of plasminogen to plasmin and extracellular matrix (ECM) degradation, directly controls cell adhesion, differentiation, proliferation, and migration through non-proteolytic mechanisms.[49,50]

It has been established that in the classic process following infection or injury, macrophages play a key role as regulators of inflammation. However, if the inflammatory response of macrophages is not properly controlled, it may lead to severe diseases such as atherosclerosis,[51] rheumatoid arthritis (RA), vascular injury, and cancer.[52] Accordingly, to moderate inflammation, macrophages have been targeted for specific ablation, inhibition of infiltration, and reduction of the release of pro-inflammatory cytokines. In this work, we demonstrated for the first time that AuNPs-SS were able to modulate the inflammatory response induced by LPS in murine macrophages by significantly reducing the IL1-β and IL-6 cytokine levels. It is known that macrophages isolated from chronic wounds in diabetic patients exhibit a proinflammatory phenotype with the release of IL-1β, MMP-9, TNF-α, and IL-6. In a recent study, Mirza and co-workers[53] showed that IL-1β sustains the proinflammatory macrophage phenotype observed in poorly healing wounds of humans and mice. The authors of the study demonstrated that targeting the IL-1β pathway upregulated the expression of pro-healing factors in wounds of diabetic mice and improved the healing of these wounds. Indeed Sumbayev *et al.* reported that citrate-stabilized gold nanoparticles were able to down-regulate the inflammatory process by selectively targeting the IL-1β dependent pathway.[54]

We also observed a massive drop in the inducible nitric oxide synthase (iNOS) levels, which is essential for macrophage activation and thus for cytokine release. Regulation of iNOS gene expression is, through transcriptional regulation, particularly influenced by NF-κB activation. Indeed, in mice, the iNOS gene promoter contains two NF-κB binding sites, both of which need to be bound in order to get full induction of iNOS by LPS stimulation. In conclusion, our findings demonstrated that AuNPs-SS can promote effective wound healing and may pave the way for accelerating the regeneration of difficult-to-heal wounds. A more in-depth understanding of the effects of NPs on macrophage activation may lead to a more potent and efficient control of inflammatory-related diseases.

Conflicts of interest

There are no conflicts to declare.

Acknowledgements

We gratefully acknowledge Mr Sergio Nuzzo for the skillful and excellent technical assistance, and Francesco Paolo Perrotta and Francesca D'Andretta, Società Agricola Dap di Francesco Paolo Perrotta & C. S.a.s – *via* Diego Rapolla, – 85029 Venosa (Potenza, Basilicata, Italy), for the snail slime production and Patrizia Iannece for her technical support, provided for mass spectrometry analysis. This research was supported by the Italian Ministry for Education, University and Research (MIUR) under grant PONa3_00369 – ''Laboratorio SISTEMA''.

References

1 P. Thangavel, R. Kannan, B. Ramachandran, G. Moorthy, L. Suguna and V. Muthuvijayan, Development of reduced graphene oxide (rGO)-isabgol nanocomposite dressings for enhanced vascularization and accelerated wound healing in normal and diabetic rats, *J. Colloid Interface Sci.*, 2018, **517**, 251–264, DOI: 10.1016/j.jcis.2018.01.110.

2 A. J. Singer and R. A. F. Clark, Cutaneous Wound Healing, *N. Engl. J. Med.*, 1999, **341**, 738–746, DOI: 10.1056/NEJM199909023411006.

3 K. Shanmugapriya and H. W. Kang, Engineering pharmaceutical nanocarriers for photodynamic therapy on wound healing: review, *Mater. Sci. Eng., C*, 2019, **105**, 110110, DOI: 10.1016/j.msec.2019.110110.

4 R. Rajakumari, T. Volova, O. S. Oluwafemi, S. Rajeshkumar, S. Thomas and N. Kalarikkal, Nano formulated proanthocyanidins as an effective wound healing component, *Mater. Sci. Eng., C*, 2020, **106**, 110056, DOI: 10.1016/j.msec.2019.110056.

5 N. B. Menke, K. R. Ward, T. M. Witten, D. G. Bonchev and R. F. Diegelmann, Impaired wound healing, *Clin. Dermatol.*, 2007, **25**, 19–25, DOI: 10.1016/j.clindermatol.2006.12.005.

6 J. E. Kim, J. Lee, M. Jang, M. H. Kwak, J. Go, E. K. Kho, S. H. Song, J. E. Sung, J. Lee and D. Y. Hwang, Accelerated healing of cutaneous wounds using phytochemically stabilized gold nanoparticle deposited hydrocolloid membranes, *Biomater. Sci.*, 2015, **3**, 509–519, DOI: 10.1039/C4BM00390J.

7 A. Pan, M. Zhong, H. Wu, Y. Peng, H. Xia, Q. Tang, Q. Huang, L. Wei, L. Xiao and C. Peng, Topical Application of Keratinocyte Growth Factor Conjugated Gold Nanoparticles Accelerate Wound Healing, *Nanomedicine*, 2018, **14**, 1619–1628, DOI: 10.1016/j.nano.2018.04.007.

8 M. Ovais, I. Ahmad, A. T. Khalil, S. Mukherjee, R. Javed, M. Ayaz, A. Raza and Z. K. Shinwari, Wound healing applications of biogenic colloidal silver and gold nanoparticles: recent trends and future prospects, *Appl. Microbiol. Biotechnol.*, 2018, **102**, 4305–4318, DOI: 10.1007/s00253-018-8939-z.

9 J. Du and K. K. Y. Wong, 9-Nanomaterials for Wound Healing: Scope and Advances, in *Micro Nano Technologies*, ed. W. Cui and X. B. T.-T. B. Zhao, Elsevier, 2019, pp. 211–230, DOI: 10.1016/B978-0-12-815341-3.00009-2.

10 A. C. Barai, K. Paul, A. Dey, S. Manna, S. Roy, B. G. Bag and C. Mukhopadhyay, Green synthesis of Nerium oleander-conjugated gold nanoparticles and study of its in vitro anticancer activity on MCF-7 cell lines and catalytic activity, *Nano Convergence*, 2018, **5**, 10, DOI: 10.1186/s40580-018-0142-5.

11 N. K. Rajendran, S. S. D. Kumar, N. N. Houreld and H. Abrahamse, A review on nanoparticle based treatment for wound healing, *J. Drug Delivery Sci. Technol.*, 2018, **44**, 421–430, DOI: 10.1016/j.jddst.2018.01.009.

12 J.-G. Leu, S.-A. Chen, H.-M. Chen, W.-M. Wu, C.-F. Hung, Y.-D. Yao, C.-S. Tu and Y.-J. Liang, The effects of gold nanoparticles in wound healing with antioxidant epigallocatechin gallate and α-lipoic acid, *Nanomedicine*, 2012, **8**, 767–775, DOI: 10.1016/j.nano.2011.08.013.

13 Z. Molnár, V. Bódai, G. Szakacs, B. Erdélyi, Z. Fogarassy, G. Sáfrán, T. Varga, Z. Kónya, E. Tóth-Szeles, R. Szűcs and I. Lagzi, Green synthesis of gold nanoparticles by thermophilic filamentous fungi, *Sci. Rep.*, 2018, **8**, 3943, DOI: 10.1038/s41598-018-22112-3.

14 E. Ismail, A. Saqer, E. Assirey, A. Naqvi and R. Okasha, Successful Green Synthesis of Gold Nanoparticles using a Corchorus olitorius Extract and Their Antiproliferative Effect in Cancer Cells, *Int. J. Mol. Sci.*, 2018, **19**, 2612, DOI: 10.3390/ijms19092612.

15 G. Ghodake, C.-Y. Eom, S. W. Kim and E. Jin, Biogenic Nano-Synthesis; towards the Efficient Production of the Biocompatible Gold Nanoparticles, *Bull. Korean Chem. Soc.*, 2010, **31**(10), 2771–2775, DOI: 10.5012/bkcs.2010.31.10.2771.

16 R. Vijayan, S. Joseph and B. Mathew, Indigofera tinctoria leaf extract mediated green synthesis of silver and gold nanoparticles and assessment of their anticancer, antimicrobial, antioxidant and catalytic properties, *Artif. Cells, Nanomed., Biotechnol.*, 2018, **46**, 861–871, DOI: 10.1080/21691401.2017.1345930.

17 Z. E. Jiménez-Pérez, P. Singh, Y.-J. Kim, R. Mathiyalagan, D.-H. Kim, M. H. Lee and D. C. Yang, Applications of Panax ginseng leaves-mediated gold nanoparticles in cosmetics relation to antioxidant, moisture retention, and whitening effect on B16BL6 cells, *J. Ginseng Res.*, 2018, **42**, 327–333, DOI: 10.1016/j.jgr.2017.04.003.

18 J. Gubitosa, V. Rizzi, A. Lopedota, P. Fini, A. Laurenzana, G. Fibbi, F. Fanelli, A. Petrella, V. Laquintana, N. Denora, R. Comparelli and P. Cosma, One pot environmental friendly synthesis of gold nanoparticles using Punica Granatum Juice: a novel antioxidant agent for future dermatological and cosmetic applications, *J. Colloid Interface Sci.*, 2018, **521**, 50–61, DOI: 10.1016/j.jcis.2018.02.069.

19 H. P. Borase, C. D. Patil, R. B. Salunkhe, R. K. Suryawanshi, B. K. Salunke and S. V. Patil, Phytolatex synthesized gold nanoparticles as novel agent to enhance sun protection factor of commercial sunscreens, *Int. J. Cosmet. Sci.*, 2014, **36**, 571–578, DOI: 10.1111/ics.12158.

20 C. Gonnelli, C. Giordano, U. Fontani, M. C. Salvatici and S. Ristori, Green Synthesis of Gold Nanoparticles from Extracts of Cucurbita pepo L. Leaves: Insights on the Role of Plant Ageing, in *Advances in Bionanomaterials: Lecture Notes in Bioengineering*, ed. S. Piotto, F. Rossi, S. Concilio, E. Reverchon and G. Cattaneo, Springer International Publishing, Cham, 2018, pp. 155–174, DOI: 10.1007/978-3-319-62027-5_14.

21 A. S. Harti, S. D. Sulisetyawati, A. Murharyati, M. Oktariani and I. B. Wijayanti, The Effectiveness of Snail Slime and Chitosan in Wound Healing, *Int. J. Pharma Med. Biol. Sci.*, 2016, **5**, 76–80.

22 T. N. Hatuikulipi, M. Kouachi, L. E. Bouchetob and D. Naimi, Preventive effect of Helix aspersa slime against experimentally chemo-induced colitis in rat, *Der Pharm. Lett.*, 2016, **8**, 200–206.

23 R. Conte, Recent advances on nano delivery of Helix mucus pharmacologically active components, *Int. J. Nano Dimens.*, 2016, **7**, 181–185, DOI: 10.7508/ijnd.2016.03.001.

24 C. Ellijimi, M. Ben Hammouda, H. Othman, W. Moslah, J. Jebali, H. Ben Mabrouk, M. Morjen, M. Haoues, J. Luis, N. Marrakchi, K. Essafi-Benkhadir and N. Srairi-Abid, Helix aspersa maxima mucus exhibits antimelanogenic and antitumoral effects against melanoma cells, *Biomed. Pharmacother.*, 2018, **101**, 871–880, DOI: 10.1016/j.biopha.2018.03.020.

25 S. G. Fabi, J. L. Cohen, J. D. Peterson, M. G. Kiripolsky and M. P. Goldman, The Effects of Filtrate of the Secretion of the Cryptomphalus Aspersa on Photoaged Skin, *J. Drugs Dermatol.*, 2013, **12**, 453–457.

26 M. J. Tribó-Boixareu, C. Parrado-Romero, B. Rais, E. Reyes, M. A. Vitale-Villarejo and S. González, Clinical and Histological Efficacy of a Secretion of the Mollusk Cryptomphalus aspersa in the Treatment of Cutaneous Photoaging, *Cosmet. Dermatol.*, 2009, **22**, 247–252.

27 S. Greistorfer, W. Klepal, N. Cyran, A. Gugumuck, L. Rudoll, J. Suppan and J. von Byern, Snail mucus – glandular origin and composition in Helix pomatia, *Zoology*, 2017, **122**, 126–138, DOI: 10.1016/j.zool.2017.05.001.

28 J. Gubitosa, V. Rizzi, P. Fini and P. Cosma, Hair Care Cosmetics: From Traditional Shampoo to Solid Clay and Herbal Shampoo, A Review, *Cosmetics*, 2019, **6**(1), 13, DOI: 10.3390/cosmetics6010013.

29 M. Soto, M. Parada, E. Falqué and H. Domínguez, Personal-Care Products Formulated with Natural Antioxidant Extracts, *Cosmetics*, 2018, **5**, 13, DOI: 10.3390/cosmetics5010013.

30 R. El Backly, V. Ulivi, L. Tonachini, R. Cancedda, F. Descalzi and M. Mastrogiacomo, Platelet Lysate Induces In Vitro Wound Healing of Human Keratinocytes Associated with a Strong Proinflammatory Response, *Tissue Eng., Part A*, 2011, **17**, 1787–1800, DOI: 10.1089/ten.tea.2010.0729.

31 X. Yin, S. Chen and A. Wu, Green chemistry synthesis of gold nanoparticles using lactic acid as a reducing agent, *Micro Nano Lett.*, 2010, **5**, 270–273, DOI: 10.1049/mnl.2010.0117.

32 V. E. Golmoraj, M. Reza Khoshayand, M. Amini, K. Mollazadeh Moghadamd, G. Amin and A. Reza Shahverdi, The surface chemistry and stability of gold nanoparticles prepared using methanol extract of Eucalyptus camaldulensis, *J. Exp. Nanosci.*, 2011, **6**, 200–208, DOI: 10.1080/17458080.2010.489581.

33 D. R. Skingsley, A. J. White and A. Weston, Analysis Of Pulmonate Mucus By Infrared Spectroscopy, *J. Molluscan Stud.*, 2000, **66**, 363–372, DOI: 10.1093/mollus/66.3.363.

34 Y. Tan, Y. Li and D. Zhu, Fabrication of Gold Nanoparticles Using a Trithiol (Thiocyanuric Acid) as the Capping Agent, *Langmuir*, 2002, **18**, 3392–3395, DOI: 10.1021/la011612f.

35 X. Li, Y. Li, Y. Tan, C. Yang and Y. Li, Self-Assembly of Gold Nanoparticles Prepared with 3,4-Ethylenedioxythiophene as

Reductant, *J. Phys. Chem. B*, 2004, **108**, 5192–5199, DOI: 10.1021/jp0356618.

36 J. Xie, J. Y. Lee and D. I. C. Wang, Synthesis of Single-Crystalline Gold Nanoplates in Aqueous Solutions through Biomineralization by Serum Albumin Protein, *J. Phys. Chem. C*, 2007, **111**, 10226–10232, DOI: 10.1021/jp0719715.

37 M. P. Casaletto, A. Longo, A. Martorana, A. Prestianni and A. M. Venezia, XPS study of supported gold catalysts: the role of Au0 and Au + δ species as active sites, *Surf. Interface Anal.*, 2006, **38**, 215–218, DOI: 10.1002/sia.2180.

38 C. S. Love, V. Chechik, D. K. Smith, K. Wilson, I. Ashworth and C. Brennan, Synthesis of gold nanoparticles within a supramolecular gel-phase network, *Chem. Commun.*, 2005, 1971–1973, DOI: 10.1039/B418190E.

39 J.-P. Sylvestre, S. Poulin, A. V. Kabashin, E. Sacher, M. Meunier and J. H. T. Luong, Surface Chemistry of Gold Nanoparticles Produced by Laser Ablation in Aqueous Media, *J. Phys. Chem. B*, 2004, **108**, 16864–16869, DOI: 10.1021/jp047134.

40 T. Fujigaya, C. Kim, Y. Hamasaki and N. Nakashima, Growth and Deposition of Au Nanoclusters on Polymer-wrapped Graphene and Their Oxygen Reduction Activity, *Sci. Rep.*, 2016, **6**, 21314, DOI: 10.1038/srep21314.

41 S. Engin, V. Trouillet, C. M. Franz, A. Welle, M. Bruns and D. Wedlich, Benzylguanine Thiol Self-Assembled Monolayers for the Immobilization of SNAP-tag Proteins on Microcontact-Printed Surface Structures, *Langmuir*, 2010, **26**, 6097–6101, DOI: 10.1021/la904829y.

42 K. Artyushkova and P. Atanassov, X-Ray Photoelectron Spectroscopy for Characterization of Bionanocomposite Functional Materials for Energy-Harvesting Technologies, *ChemPhysChem*, 2013, **14**, 2071–2080, DOI: 10.1002/cphc.201300037.

43 F. Fanelli, F. Fracassi, A. Lapenna, V. Angarano, G. Palazzo and A. Mallardi, Atmospheric Pressure Cold Plasma: A Friendly Environment for Dry Enzymes, *Adv. Mater. Interfaces*, 2018, **5**, 1801373, DOI: 10.1002/admi.201801373.

44 S. E. Glassford, B. Byrne and S. G. Kazarian, Recent applications of ATR FTIR spectroscopy and imaging to proteins, *Biochim. Biophys. Acta, Proteins Proteomics*, 2013, **1834**, 2849–2858, DOI: 10.1016/j.bbapap.2013.07.015.

45 A. Barth, Infrared spectroscopy of proteins, *Biochim. Biophys. Acta, Bioenerg.*, 2007, **1767**, 1073–1101, DOI: 10.1016/j.bbabio.2007.06.004.

46 O. Akturk, K. Kismet, A. C. Yasti, S. Kuru, M. E. Duymus, F. Kaya, M. Caydere, S. Hucumenoglu and D. Keskin, Collagen/gold nanoparticle nanocomposites: a potential skin wound healing biomaterial, *J. Biomater. Appl.*, 2016, **31**, 283–301, DOI: 10.1177/0885328216644536.

47 R. Pascale, G. Bianco, T. R. I. Cataldi, P.-S. Kopplin, F. Bosco, L. Vignola, J. Uhl, M. Lucio and L. Milella, Mass spectrometry-based phytochemical screening for hypoglycemic activity of Fagioli di Sarconi beans (Phaseolus vulgaris L.), *Food Chem.*, 2018, **242**, 497–504, DOI: 10.1016/j.foodchem.2017.09.091.

48 P. Dolashka, A. Dolashki, L. Velkova, S. Stevanovic, L. Molin, P. Traldi, R. Velikova and W. Voelter, Bioactive compounds isolated from garden snails, *J. Biosci. Biotechnol.*, 2015, 147–155.

49 S. D'Alessio, L. Gerasi and F. Blasi, uPAR-deficient mouse keratinocytes fail to produce EGFR-dependent laminin-5, affecting migration in vivo and in vitro, *J. Cell Sci.*, 2008, **121**, 3922–3932, DOI: 10.1242/jcs.037549.

50 F. Blasi and P. Carmeliet, uPAR: a versatile signalling orchestrator, *Nat. Rev. Mol. Cell Biol.*, 2002, **3**, 932–943, DOI: 10.1038/nrm977.

51 H. M. Wilson, Macrophages heterogeneity in atherosclerosis – implications for therapy, *J. Cell. Mol. Med.*, 2010, **14**, 2055–2065, DOI: 10.1111/j.1582-4934.2010.01121.x.

52 M. Talekar, T.-H. Tran and M. Amiji, Translational Nano-Medicines: Targeted Therapeutic Delivery for Cancer and Inflammatory Diseases, *AAPS J.*, 2015, **17**, 813–827, DOI: 10.1208/s12248-015-9772-2.

53 R. E. Mirza, M. M. Fang, W. J. Ennis and T. J. Koh, Blocking Interleukin-1β Induces a Healing-Associated Wound Macrophage Phenotype and Improves Healing in Type 2 Diabetes, *Diabetes*, 2013, **62**, 2579–2587, DOI: 10.2337/db12-1450.

54 V. V. Sumbayev, I. M. Yasinska, C. P. Garcia, D. Gilliland, G. S. Lall, B. F. Gibbs, D. R. Bonsall, L. Varani, F. Rossi and L. Calzolai, Gold Nanoparticles Downregulate Interleukin-1β-Induced Pro-Inflammatory Responses, *Small*, 2013, **9**, 472–477, DOI: 10.1002/smll.201201528.

